Cryogenics 50 (2010) 373–380

Contents lists available at ScienceDirect

Cryogenics

journal homepage: www.elsevier.com/locate/cryogenics

Hydrodynamic parameters of mesh fillers relevant to miniature regenerative cryocoolers

E.C. Landrum [a], T.J. Conrad [a,*], S.M. Ghiaasiaan [a], Carl S. Kirkconnell [b]

[a] G.W. Woodruff School of Mechanical Engineering, Georgia Institute of Technology, Atlanta, GA 30332, USA
[b] Iris Technology Corporation, Irvine, CA 92614, USA

ARTICLE INFO

Article history:
Received 28 May 2009
Received in revised form 12 January 2010
Accepted 27 January 2010

Keywords:
Oscillatory flow
Steady flow
Friction factor
Darcy permeability
Forchheimer's inertial coefficient

ABSTRACT

Directional hydrodynamic parameters of two fine-mesh porous materials that are suitable for miniature regenerative cryocoolers were studied under steady and oscillating flows of helium. These materials included stacked discs of #635 stainless steel (wire diameter of 20.3 μm) and #325 phosphor bronze (wire diameter of 35.6 μm) wire mesh screens, which are among the commercially available fillers for use in small-scale regenerators and heat exchangers, respectively. Experiments were performed in test sections in which pressure variations across these fillers, in the axial and lateral (radial) directions, were measured under steady and oscillatory flows. The directional permeability and Forchheimer's inertial coefficient were then obtained by using a Computational Fluid Dynamics (CFD)-assisted method. The oscillatory flow experiments covered a frequency range of 50–200 Hz. The results confirmed the importance of anisotropy in the mesh screen fillers, and indicated differences between the directional hydrodynamic resistance parameters for steady and oscillating flow regimes.

1. Introduction

In the past decade, research and development has sought to reduce the size and weight of cryocoolers while maintaining their relative system performance [1–13]. There are a number of methods and reliable tools available for design, modeling and optimization of pulse tube refrigerators (PTR) and Stirling expanders; however, their accuracy at predicting processes of small scale devices is uncertain. These models often utilize one-dimensional governing equations and empirical relationships obtained from standard scale devices. Computational Fluid Dynamics (CFD)-based methods have recently been shown to be a reliable technique for designing and predicting the performance of Stirling and PTR systems.

CFD modeling of PTRs requires realistic closure relations, particularly with respect to the hydrodynamic and thermal transport processes for the porous segments of PTR systems, which are employed in their regenerators and heat exchangers. Recent publications have established hydrodynamic parameters and correlations for several common regenerator fillers [13–18]. However, these materials are not suitable for miniature cryocoolers due to their relatively coarse structure. The objective of this study was thus to determine the hydrodynamic parameters for two important and commercially available materials suitable for use in miniature cryocoolers; stacked screens of #635 stainless steel wire mesh and #325 phosphor bronze wire mesh.

Accurate prediction of flow phenomena in porous media requires pore-level direct simulation [19–23]. Such simulations are prohibitively computationally intensive, however. Instead, in CFD simulations of cryocoolers, volume-averaged conservation equations are applied to porous regions, which capture the macroscopic fluid behavior without solving for the detailed fluid motion and transport phenomena at the microscopic scale [13,18,23,30]. Empirical correlations which include the Darcy permeability and Forchheimer's inertial coefficient are required for the closure of macroscopic momentum conservation equations in these simulations.

The porous structures which are employed in cryocoolers are usually composed either of stacked screens or micro fabricated structures, which are often anisotropic. As a result, the hydrodynamic parameters which characterize them are anisotropic and closure relations are needed at least for the axial and lateral (radial) directions. Recent studies [13,24,25] have also shown that hydrodynamic parameters may vary when the porous structures are subjected to steady or oscillating flows.

This paper describes the measurements of the directional hydrodynamic parameters of steady and oscillatory flow of helium through stacked screens of #635 stainless steel and #325 phosphor bronze mesh fillers using a CFD-assisted methodology. Directional hydrodynamic resistance parameters are determined through measurements of fluid mass flow rate and pressure drop across

* Corresponding author.
E-mail address: Ted_Conrad@gatech.edu (T.J. Conrad).

0011-2275/$ - see front matter © 2010 Elsevier Ltd. All rights reserved.
doi:10.1016/j.cryogenics.2010.01.017

Nomenclature

$\overline{\overline{C}}$, C	inertial resistance coefficient tensor, scalar (m^{-1})
c_f	Forchheimer's inertial coefficient (–)
$\overline{\overline{D}}$, D	viscous resistance coefficient tensor, scalar (m^{-2})
e	total specific energy (J/kg)
f	friction factor (–)
f	frequency (Hz)
$\vec{F}$	volumetric force vector (N/m^3)
k	thermal conductivity (W/m K)
K	Darcy permeability (m^2)
l	length of sample (m)
Re	Reynolds number (–)
P	pressure (Pa)
t	time (s)
T	temperature (K)
u	superficial velocity (m/s)
$\vec{v}$	physical velocity vector (m/s)
Z	pressure amplitude (Pa)

Greek symbols

ε	porosity (–)
μ	dynamic viscosity (kg/m s)
ω	angular frequency (rad/s)
φ	phase angle (rad)
ρ	density (kg/m^3)
$\overline{\overline{\tau}}$	viscous stress tensor (Pa)

Subscripts

bf	body force
i	related to direction *i*
f	fluid
sol	solid

the porous media. By simulating the experimental test setup using CFD, model viscous and inertial resistances are iteratively adjusted until agreement is reached between experimental results and simulated predictions. This method of determining the hydrodynamic characteristics under steady and periodic flow conditions, namely the quantification of hydrodynamic parameters that would lead to agreement between experimental data and the predictions of detailed, numerical simulations, was proposed by Harvey [18]. Cha [13] and Clearman [16] further developed this process through the incorporation of detailed, two-dimensional CFD analyses.

2. Experiments

Experiments were performed separately for the axial and radial directions under steady and oscillatory flows. Accordingly, each direction and flow regime utilized distinctive samples, housing units, instrumentation and methodologies. All setups employed ultra high purity helium as the working fluid. Experimental systems were purged of air and other contaminants and test runs were only performed after strict assurance of a hermetically sealed setup. All testing was conducted at ambient temperatures of approximately 300 K.

Wire cloth material was supplied by TWP Inc. (Berkeley, CA) and test samples were machined using a punching operation. The #635 stainless steel and #325 phosphor bronze mesh materials possess a plain square weave pattern where perpendicular wires are woven into a simple over and under configuration. Each mesh is characterized by the number of parallel strands of wires it has per inch within its matrix; square weave patterns have the same number in each direction. A random orientation was adopted when stacking the screens and a uniform, high packing density was obtained in order to mimic industry standards.

The intrinsic properties of the investigated porous samples are summarized in Table 1. Axial test samples consisted of 4 mm discs stacked within a housing unit while the radial samples consisted of stacks of annular cutouts. Sample porosities were calculated using the occupied volume of the specimen housing, aggregate sample mass and an average material density. Experimental setups for each flow direction used the same porous samples. Thus, for axial flow both the steady and oscillatory flow parameterization tests employed the same axial test samples. The same idea pertains to radial testing.

2.1. Steady flow experimentation

The experimental and computational procedures for determining the hydrodynamic steady, axial and radial flow resistances were very similar. Equipment employed in both cases was identical with the exception of the porous samples, housing units and associated fittings. Fig. 1 shows a diagram of the steady flow test setups. The test sections used for axial and radial flow tests are displayed in Fig. 3a, and b, respectively.

The steady flow experimental apparatus consisted of a helium supply tank and pressure regulator, two static pressure transducers, a mass flow meter and a specially designed test section containing the porous sample. The mass flow meter (Sierra Instruments, TopTrak model 826) was calibrated for helium at atmospheric conditions and had a range of 0–1.5 g/s with an accuracy of ±1.5% of full scale. The pressure sensors (Paine Electronics, series 210-10) have an accuracy of ±0.35% of full scale with a range of 0–3.45 MPa. Pressure signals were amplified though a signal conditioner (Omega DMD-465WB) where a linear calibration was applied across its full range using a dial pressure gauge. Pressure

Table 1
Test sample details.

Porous media	Sample geometry			Mesh geometry			Measured porosity (–)
	ID (mm)	OD (mm)	Length (mm)	Wire diameter (μm)	Thickness (μm)	Pore size (μm)	
Axial samples							
#325 Phosphor bronze	N/A	4.0	12.7	35.6	71.1	43	0.6738
#635 Stainless steel	N/A	4.0	12.7	20.3	40.6	20	0.6312
Radial samples							
#325 Phosphor bronze	4.0	20.0	3.4	35.6	71.1	43	0.6702
#635 Stainless steel	4.0	20.0	6.1	20.3	40.6	20	0.6304

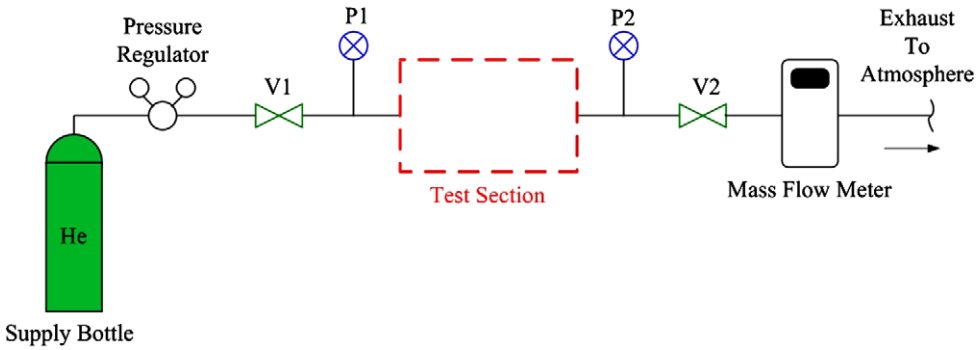

Fig. 1. Steady flow experimental setup.

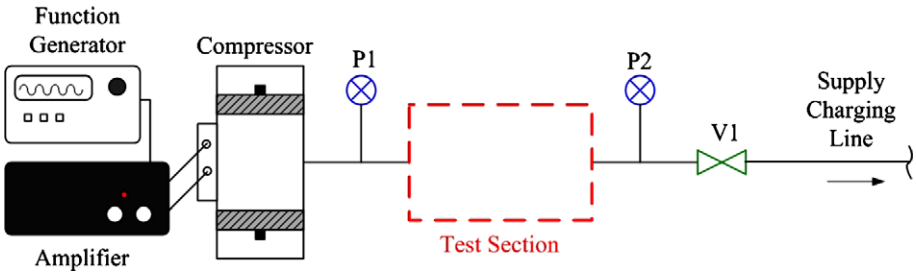

Fig. 2. Oscillatory flow experimental setup.

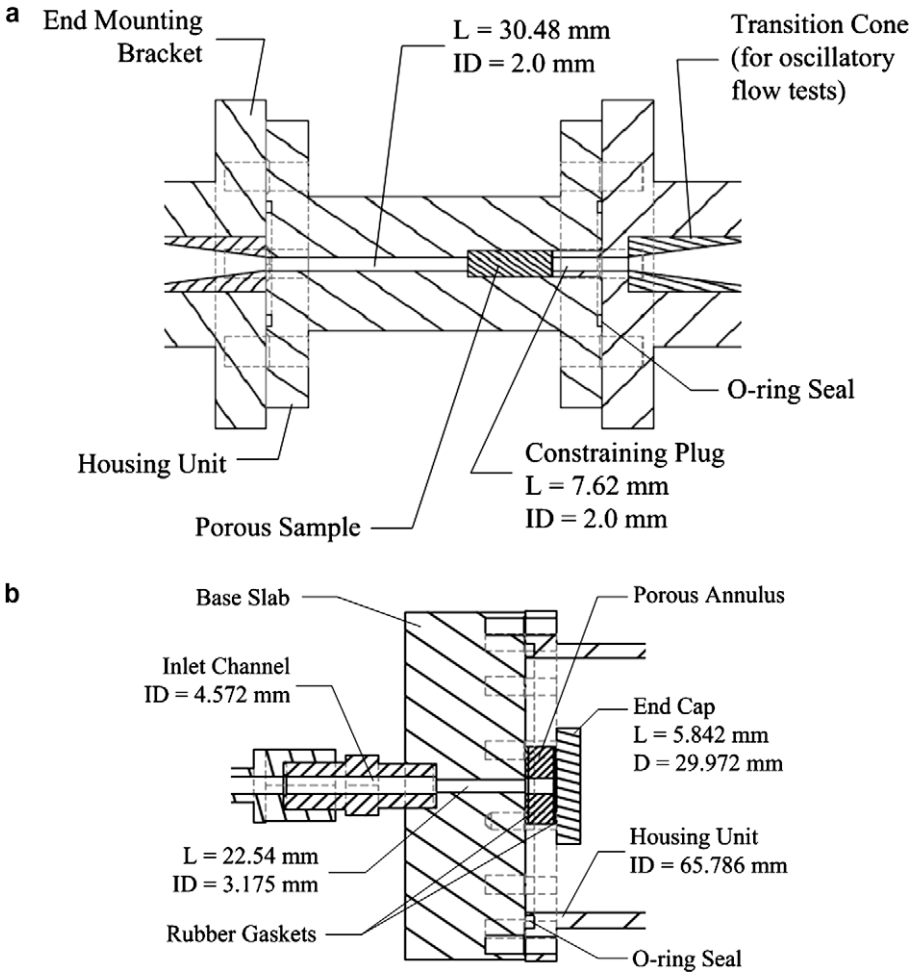

Fig. 3. (a) Axial flow test section. (b) Radial flow test section.

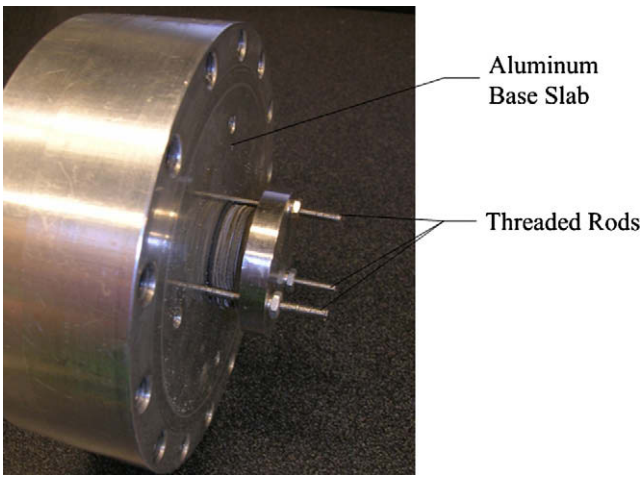

Fig. 4. Photograph of #635 stainless steel radial test sample mounted within housing unit.

and mass flow rate measurements were read as analog voltage signals via handheld digital multimeters.

The axial flow test section (Fig. 3a) which houses the porous media is a hollow aluminum cylinder with two inner diameters separated by a step change. A 2.0 mm passage opens up to a 4.013 mm diameter channel which contains the stacked screens. End pieces bolted onto flanges located on either side of the test section constrain the axial sample and provide a mount for one of the static pressure transducers. The test sample and housing were designed with a large aspect ratio (length-to-diameter ratio) of 3.2 to ensure that the flow within the porous structure is predominately in the axial direction. Strict tolerances used in fabrication ensured a negligible clearance between the stacked screens and the test section's inner diameter.

The radial flow test section (Fig. 3b) contains stacks of annular screens constrained between an aluminum slab and end cap which are supported by three threaded rods. Thin rubber discs were placed between the screens and the slab and end cap to eliminate the possibility of low-resistance paths between the screens and these parts. A photograph of a radial sample mounted in the housing unit is shown in Fig. 4. Radial test samples were designed to produce a predominately radial velocity component within the porous structure. The length of the annular porous sample is adjusted by tightening the nuts on the threaded rods to closely match the porosity of its axial counterpart. By making the porosities nearly equal for both radial and axial samples, a complete parameterization could be made for each material at the tested porosity.

The steady flow test procedures were identical for the axial and radial flow directions. Valves, V1 and V2 and pressure transducers, P1 and P2 were respectively located upstream and downstream of the porous test section. During each steady flow test, helium flowed from the supply bottle, through V1 and entered the test section. The fluid then exited the test section through valve V2 where it was straightened before passing through the mass flow meter and exhausting to the atmosphere. With V2 closed and V1 open the system was charged to a gage pressure of 2.76 MPa. V2 was then modulated to offer a range of mass flows up to 1.5 g/s. Static pressures at locations designated by P1 and P2 were recorded for discrete mass flow rates. Multiple test runs were performed for each filler material in the axial and radial flow directions. The maximum allowable pressure drop across the porous section was limited to 0.7 MPa to prevent large fluctuations in the mean pressure within the sample and therefore avoiding the complications caused by large variations in fluid density.

Pressure drops recorded between sensors P1 and P2 are plotted as a function of mass flow rate for each test sample. Polynomial curves of the experimental data are generated with a zero intercept. The resulting equation would then act as a guide for defining the boundary conditions used for the iterative CFD analysis.

2.2. Oscillatory flow experimentation

The experimental and computational procedures for determining the hydrodynamic oscillatory axial and radial flow resistances were also similar. The same instrumentation was utilized in both setups with the exception of the porous samples, housing units and associated fittings. Oscillatory flow test sections consisted of the same sample pieces and housing used in steady flow testing; however, the mounting brackets were modified to accommodate the dynamic sensors. A schematic of oscillatory flow test setup is shown in Fig. 2.

The oscillatory flow setup (Fig. 2) included a tactical compressor (Hughes Aircraft Condor), a function generator (HP-Agilent 33120A), data acquisition control unit (HP-Agilent 3852A), amplifier (Crown DC-300A series II), two high frequency dynamic pressure transducers (PCB Piezotronics 101A05), and the test section containing the porous sample. The dynamic pressure sensors had a resolution of 0.014 kPa. An iron core transformer was also utilized between the amplifier and compressor to further increase the current output of the amplifier.

Increased operating frequencies and fill pressures are core design requirements for miniature cryocoolers. Consequently, data was taken for each sample at seven distinct frequencies in the 50–200 Hz range, in 25 Hz intervals, at nominal charge pressures of 2.86 and 3.55 MPa. Low flow data was first obtained at 50 Hz for each charge pressure and used to determine the viscous resistances. Subsequently, high flow data taken at each pressure and frequency was used to determine the sample inertial resistances.

The oscillatory flow experimental setup (Fig. 2) was a closed system bounded by the compressor and valve, V1. During each test, pressure sensors located on either end of the porous test section (Fig. 3b) sampled periodic waveforms which were then represented by their first three harmonics using a Fast Fourier Transform (FFT). A mathematical interpretation of the first three terms of the FFT as used in the analysis is,

$$P_{osc} = Z_1 \cos(\omega t + \phi_1) + Z_2 \cos(2\omega t + \phi_2) + Z_3 \cos(3\omega t + \phi_3) \quad (1)$$

where amplitudes are expressed as Z_j and the phase angles are represented with ϕ_j, and

$$\omega = 2\pi f \quad (2)$$

Past experience has shown that this method of representing the pressure signals is quite accurate [13]. The pressure waveform recorded at P1 was applied as an inlet boundary condition for iterative CFD analysis.

Two separate housing units were used in the oscillatory radial flow experiments. A smaller volume of 95 cm^3 was originally used in the setup; however, certain frequencies would produce non-sinusoidal waveforms at the P2 location. As a result, a larger shroud of 289 cm^3 was employed to avoid this form of acoustical interference. All the experimental data discussed here are related to the latter larger test section.

3. Computational analysis and data interpretation

The CFD-assisted method for the analysis of the tests and interpretation of data will be discussed only briefly here. More details about the methodology can be found in [13,16].

3.1. Porous media formulation

The mass, momentum, and energy equations are:

$$\frac{\partial}{\partial t}(\varepsilon\rho) + \nabla\cdot(\varepsilon\rho\,\vec{v}) = 0 \tag{3}$$

$$\frac{\partial}{\partial t}(\varepsilon\rho\,\vec{v}) + \nabla\cdot(\varepsilon\rho\,\vec{v}\,\vec{v}) = -\varepsilon\nabla P + \nabla\cdot(\varepsilon\bar{\bar{\tau}}) + \varepsilon\vec{F}_{bf} - \mu\bar{\bar{D}}\cdot\vec{v} - \frac{\bar{\bar{C}}\rho}{2}\cdot|\vec{v}|\vec{v} \tag{4}$$

$$\frac{\partial}{\partial t}(\varepsilon\rho_f e_f + (1-\varepsilon)\rho_{sol}e_{sol}) + \nabla\cdot(\varepsilon\,\vec{v}(\rho_f e_f + P)) - \nabla\cdot((\varepsilon k_f + (1-\varepsilon)k_{sol})\nabla T + \bar{\bar{\tau}}\cdot\varepsilon\,\vec{v}) = 0 \tag{5}$$

where $|\vec{v}|$ represents the absolute magnitude of the velocity vector. Since the test sections are all axisymmetric, the axial and radial directions are principal directions of the porous medium, and therefore one can write for any of these directions,

$$K_i = \frac{\varepsilon^2}{D_i} \tag{6}$$

$$c_{f_i} = \frac{C_i\sqrt{K_i}}{2\varepsilon^3} \tag{7}$$

Alternatively, a directional friction factor can be defined, whereby for steady flow [29],

$$(-\nabla P)_i = \frac{1}{2}\frac{f_i}{\sqrt{K_i}}\rho|\vec{u}|u_i = \frac{\mu}{K_i}u_i + \frac{c_{f,i}\rho}{\sqrt{K_i}}|\vec{u}|u_i \tag{8}$$

The friction factor is often correlated in terms of a Reynolds number, defined as

$$\mathrm{Re}_{K,i} = \frac{\rho|\vec{u}|\sqrt{K_i}}{\mu} \tag{9}$$

$$f_i = \frac{2}{\mathrm{Re}_{K,i}} + 2c_f \tag{10}$$

3.2. Computational methods

For this investigation, the Fluent software package was used [31]. All simulations were two-dimensional, axisymmetric representations of the experimental test sections and their vicinities. Nodalized grids were created using the Gambit [26] software package and then imported into Fluent. Grid independence studies were performed by testing multiple grids for each case to determine how nodal spacing affected the output variables Meshes with the lowest cell count and largest spacing which provided negligible change in results as compared with finer mesh schemes were employed. Typically, variations in simulated pressure amplitude of less than 1% when the mesh spacing was halved were considered negligible. For the oscillatory flow simulations, time steps were selected for each frequency to provide at least 190 steps per period of the sinusoidal input function. Further halving the time step was tested for a limited number of cases, which resulted in changes of less than 0.2% in the simulated pressure amplitudes.

The pure helium was modeled as an ideal gas. Open fluid volumes utilized the standard governing equations while fluid behavior within the porous media was governed by the aforementioned volume-averaged conservation equations. The walls were modeled as smooth adiabatic surfaces. Gravitational body forces were not included in the CFD analysis, since their effect was negligibly small.

Model parameters such as first or second order discretization solver techniques and pressure–velocity coupling methods were chosen for each setup to offer the best residual convergence. A universal set of convergence criteria was applied to all simulations that restricted residual values to less than 1E−7.

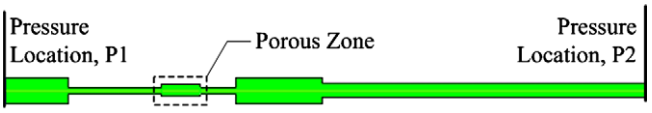

Fig. 5. Steady axial flow mesh.

The CFD code utilized input values for a porous zone's viscous and inertial resistances. It is these values that were iteratively adjusted until the simulation's predicted output variables matched that of experimental measurements. Isotropic viscous and inertial resistances were assumed when determining the hydrodynamic parameters for all cases. Although this conjecture is unrealistic, it is justifiable because the flow within the porous structure is predominately one-dimensional.

3.2.1. Steady flow analysis

As mentioned earlier, the steady flow experimentation yielded polynomial curve fits of pressure drop as a function of mass flow rate. Seven representative data points for each filler material and flow direction were chosen for CFD analysis. A single steady flow case was generated for each data point. The grid used in each case modeled the fluid control volume of the test setup geometry between the P1 and P2 pressure transducer locations. The steady axial flow grid is illustrated in Fig. 5 comprising a longitudinal length of approximately 209 mm with over 11,000 quadrilateral elements. Similarly, the steady radial flow grid resulted in 6700 quadrilateral cells.

Although the steady axial flow grids were identical for the two filler materials, the steady radial flow grids varied slightly for the different sample lengths. The rubber gaskets and threaded rods used in the radial flow experimental setups were excluded from the CFD analysis. The end cap which constrained the radial samples was included in the model and treated as an adiabatic solid interface. In steady flow through porous media, transition from laminar to turbulent flow occurs at $\mathrm{Re}_K \approx 350$ [27]. The majority of the test data was in the laminar regime. Laminar models were therefore applied for most of the simulations. However, high Reynolds numbers were encountered in some axial flow experiments. The standard k–epsilon turbulence model was employed for these cases.

The experimentally measured pressure at P2 and the inlet mass flow rate were applied as simulation boundary conditions. Initial guess values for the viscous and inertial resistances were applied to the porous zone and the model was iterated until there was agreement between the simulated and experimental pressures at P1.

For both the steady axial and radial flow cases, the viscous resistance could be established at low flow conditions when inertial effects were small. Using an iterative method, several data points with low mass flow rates were utilized to localize the viscous parameter only. Once this value had been decided, the inertial term was then determined at higher flow rates.

3.2.2. Oscillatory flow analysis

Oscillatory flow testing produced pressure waveforms for two distinct charge pressures and a range of operating frequencies. CFD cases were created to model the fluid control volume within the test section geometry, depicted in Fig. 3a and b, between the P1 pressure transducer location and the valve V1. The oscillatory axial flow mesh was comprised of 2000 cells, and the oscillatory radial flow grids contained 14,000 quadrilateral elements.

Eight separate cases for the seven distinct frequencies from 50 to 200 Hz, and a separate low flow 50 Hz, were constructed for

each filler material, flow direction and charge pressure. The aforementioned experimental measurement-based FFT pressure signals at P1 were applied as a user defined pressure inlet boundary condition for the simulations. The porous region's viscous and inertial resistances were then iteratively varied. Each simulation was continued for about ten periods until steady-periodic state was reached. Iterative simulations were repeated until pressure at the P2 location matches the experimental pressure waveform at that location.

Similar to its steady counterpart, the viscous resistance was initially determined at the 50 Hz low flow case, where inertial effects are small. Once a range of prescribed viscous resistances was established, inertial resistances were adjusted to match experimental conditions at higher flow rates.

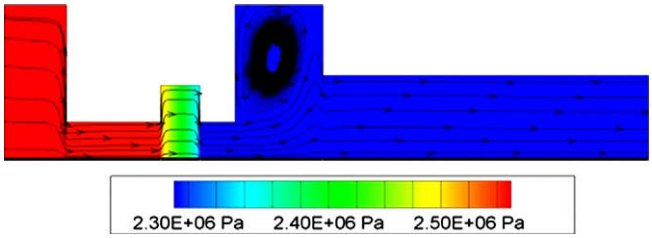

Fig. 6. Pressure contour of #325 phosphor bronze steady axial flow case at 0.546 g/s.

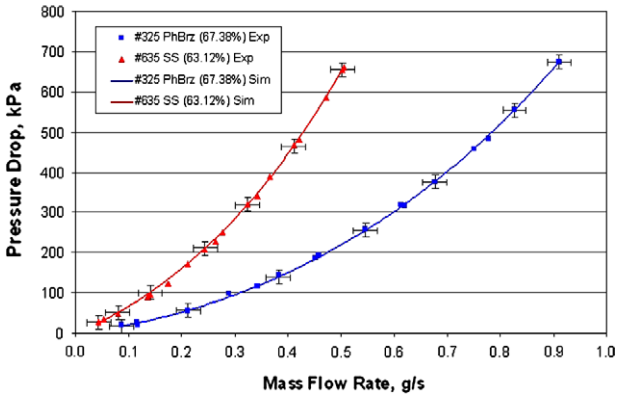

Fig. 7. Steady axial flow pressure plot.

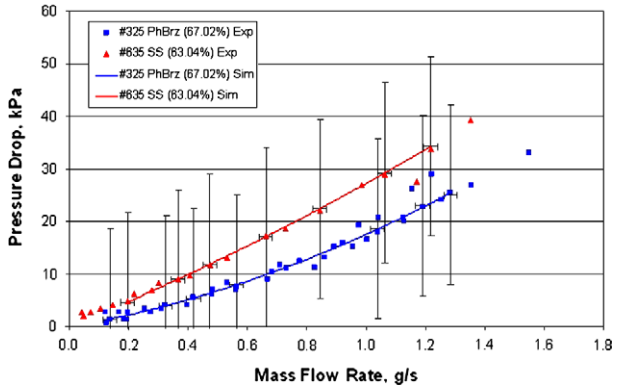

Fig. 8. Steady radial flow pressure plot.

4. Results

4.1. Steady flow

Fig. 6 shows a typical CFD-predicted pressure distribution in the test section. The contour plots in this and other similar simulations suggest that virtually all of the flow resistance can be attributed to the stacked screens of wire mesh and that other losses are small in comparison.

Figs. 7 and 8 display pressure drop as a function of mass flow rate for the two axial flow and two radial flow test samples, respectively, each for two different porosities. Discrete experimental data points are directly compared with curves representing the simulation-predicted pressure drops. The error bars represent the uncertainty associated with the experimental measurements. The combined uncertainty for static pressure drop was ±17.1 kPa while the mass flow meter yielded an uncertainty of ±0.0225 g/s.

Steady axial flow measurements were found to be very reproducible and the uncertainty remained relatively small. To determine the accuracy of the CFD-predicted pressure drops, polynomial trend lines representing the experimental data and simulated predictions were numerically compared. A maximum deviation of 4.7% occurred between the experimental and simulated pressure drops for all axial pressure drops. The average deviations were 1.3% and 2.2%, respectively, for the #325 phosphor bronze and #635 stainless steel fillers, respectively.

With a superficial lateral length of only 16 mm from the inner to outer diameters for the fluid to traverse, steady radial flow testing only produced small pressure drops across the range of mass flow rates. Fig. 8 shows the discrete measured radial pressure drops, along with curve fits representing the final simulation results. The approximately linear profile of the radial pressure drop plots would suggest a predominately Darcy or viscous flow pattern with little inertial effects. Some scatter can also be observed in the data as pressure differences approached the uncertainty associated with the transducers. Notwithstanding the large uncertainty limits, comparative analysis was performed on the experimental and simulated curve fits. A maximum deviation of 5.7% occurred between the experimental pressure drop data and the final CFD simulation results. The average deviations were 3.6% and 0.8% for the #325

Table 2
Steady flow sample hydrodynamic parameters.

Porous media	Measured porosity (–)	Viscous resistance coefficient (m^{-2})	Inertial resistance coefficient (m^{-1})	Darcy permeability (m^2)	Forchheimer's coefficient (–)
Axial samples					
#325 Phosphor bronze	0.6738	2.85 ± 0.3 E+10	27,500 ± 1500	1.593 ± 0.17 E−11	0.179 ± 0.014
#635 Stainless steel	0.6312	9.95 ± 0.4 E+10	69,000 ± 3000	4.004 ± 0.16 E−12	0.275 ± 0.013
Radial samples					
#325 Phosphor bronze	0.6702	2.85 ± 0.5 E+10	58,000 ± 7000	1.576 ± 0.29 E−11	0.382 ± 0.057
#635 Stainless steel	0.6304	1.24 ± 0.1 E+11	59,000 ± 5000	3.205 ± 0.26 E−12	0.211 ± 0.057

Table 3
Oscillatory flow sample hydrodynamic parameters.

Porous media	Charge pressure (MPa)	Viscous resistance coefficient (m^{-2})	Inertial resistance coefficient (m^{-1})	Darcy permeability (m^2)	Forchheimer's coefficient (–)
Axial samples					
#325 PhBrz (67.38%)	2.8	1.70 ± 0.2 E+10	50,000 ± 6000	2.672 ± 0.32 E−11	0.422 ± 0.056
#325 PhBrz (67.38%)	3.5	1.70 ± 0.2 E+10	50,000 ± 6000	2.672 ± 0.32 E−11	0.422 ± 0.056
#635 SS (63.12%)	2.8	9.50 ± 0.2 E+10	40,000 ± 5000	4.194 ± 0.08 E−12	0.163 ± 0.020
#635 SS (63.12%)	3.5	9.50 ± 0.2 E+10	40,000 ± 5000	4.194 ± 0.08 E−12	0.163 ± 0.020
Radial samples					
#325 PhBrz (67.02%)	2.8	2.90 ± 0.2 E+10	50,000 ± 10,000	1.549 ± 0.11 E−11	0.327 ± 0.066
#325 PhBrz (67.02%)	3.5	2.90 ± 0.2 E+10	50,000 ± 10,000	1.549 ± 0.11 E−11	0.327 ± 0.066
#635 SS (63.04%)	2.8	1.05 ± 0.05 E+11	120,000 ± 20,000	3.785 ± 0.18 E−12	0.466 ± 0.078
#635 SS (63.04%)	3.5	1.11 ± 0.05 E+11	120,000 ± 20,000	3.596 ± 0.16 E−12	0.454 ± 0.076

phosphor bronze and #635 stainless steel radial samples, respectively.

Table 2 summarizes the steady flow results, including the directional viscous and inertial resistances and their associated directional permeability and inertial coefficients for the tested sample materials. Confidence intervals for the parameters in Table 2 are estimated based upon the scatter in the data sets. For the #325 phosphor bronze filler type, as noted, the axial and radial viscous resistance parameters are approximately the same, while the inertial resistance parameters are different. For the #635 stainless steel filler, however, both resistance parameters are significantly different for the axial and radial directions.

4.2. Oscillatory flow results

The oscillatory flow experimental results with the more resistive #635 stainless steel filler produced pressure waveforms which behaved as expected, where the pressure waves at the test section exit had smaller amplitude than those at the inlet. Some of the oscillatory flow experiments with the #325 phosphor bronze filler were complicated due to acoustical interference that in some cases caused the pressure waves at the exit of the test section to have larger amplitudes than the pressure waves at inlet. The runs with acoustic interference were therefore identified and deleted from the experimental data set. These experiments were then repeated with the larger shroud volume previously described to minimize the acoustical interference. Additionally, the compressor exhibited resonance around 40 Hz and its response diminished at higher operating frequencies, thus limiting the pressure wave amplitudes in experiments at higher frequencies. A detailed discussion of these and other issues regarding the experiments can be found in [28].

Using the experimental data, an average set of directional hydrodynamic parameters was determined for each filler material and charge pressure, encompassing the range of tested frequencies. These values along with the directional permeabilities and inertial coefficients are summarized in Table 3. Confidence intervals for these oscillatory cases were estimated based upon the range of parameters providing reasonably good agreement between simulated and experimental result. Typical experimental and simulated waveforms are shown in Fig. 9, in this case for the #635 stainless steel filler in radial flow at 75 Hz and 3.55 MPa mean pressure. A comprehensive set of such plots can be found in [28]. In the figure, very good agreement can be seen between the simulated and experimental results. The average error between the measured and the final simulation-predicted pressure amplitudes at P2 were 3.7% and 3.5% for the axial and radial flow configurations, respectively. The average deviations between the measured and the final

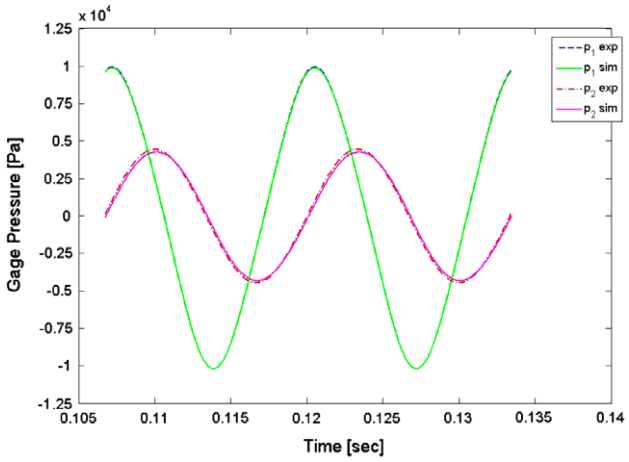

Fig. 9. Typical oscillatory flow experimental and simulated waveforms, #635 stainless steel, radial flow at 75 Hz, 3.55 MPa.

simulation-predicted phase angles at location P2 were 1.48° and 1.43° for the axial and radial flow configurations, respectively.

For three out of the four directional test samples a single set of viscous and inertial resistances could fit the experimental data for both charge pressures of 2.9 and 3.6 MPa. The exception was the #635 stainless steel filler in radial flow, for which the viscous and inertial resistance parameters differed only slightly for the two charge pressures. The experimental results thus suggest that periodic flow hydrodynamic parameters may be insensitive to the charge pressure. It is emphasized, however, that a conclusion regarding the effect of pressure on oscillatory flow hydrodynamics requires further experimental verification.

5. Concluding remarks

In this study the directional hydrodynamic parameters of #635 stainless steel and #325 phosphor bronze wire mesh screens were experimentally determined for steady and oscillating flow of room temperature helium. These two commercially available, fine-mesh porous materials suitable for miniature regenerative cryocoolers were studied under steady and oscillating flows of helium gas. In the experiments, pressure variations across test sections packed with these fillers were measured in axial and lateral (radial) directions, under steady and oscillatory flows. The directional permeability and Forchheimer's inertial coefficient were then obtained by using a Computational Fluid Dynamics (CFD)-assisted method.

The resulting coefficients were similar to those reported previously [13–16] for other, coarser mesh screens. The oscillatory flow experiments covered a frequency range of 50–200 Hz. The pore level Reynolds number Re_K varied in the range of 0.02–15. The results confirmed the importance of anisotropy in the mesh screen fillers, and indicated differences between the directional hydrodynamic resistance parameters for steady and oscillating flow regimes.

Acknowledgements

The authors appreciate the valuable contribution of Drs. Tom Crittenden and Slava Yorish (Virtual Aero Surface Technologies, Atlanta, GA) for the design and fabrication of the experimental test samples.

References

[1] Xiao JH, Yang JH, Tao ZD. Miniature double-inlet pulse tube cryocooler: design by thermoacoustic theory compared with preliminary experimental results. Adv Cryog Eng 1996;41(B):1435–41.
[2] Shire JM, Mujezinovic A, Phelan PE. Optimization of miniature pulse-tube cryocoolers. Am Soc Mech Eng, Adv Energy Syst Div 1999;39:63–7.
[3] Hou YK, Ju YL, Yan LW, Zhou Y, Liang JT. The effect of the regenerator and tube volume on the performance of high frequency miniature pulse tube refrigerators. Adv Cryog Eng 2002;47(A):723–30.
[4] Hou YK, Ju YL, Yan LW, Liang JT, Zhou Y. Experimental study on a high frequency miniature pulse tube refrigerator with inertance tube. Adv Cryog Eng 2002;47(A):731–8.
[5] Xiong LY, Kaiser G, Binneberg A. Theoretical study on a miniature Joule–Thomson & Bernoulli cryocooler. Cryogenics 2004;44(11):801–7.
[6] Zhao M-G, Wang X-L, Hou X-F, Liang J-T, Cai J-H, Zhou Y. Design and test of a 80 K miniature pulse tube cryocooler. In: Proceedings of 20th international cryogenic engineering conference; May 2004. p. 225–8.
[7] Yang X, Chung JN. Size effects on miniature Stirling cycle cryocoolers. Cryogenics 2005;45(8):537–45.
[8] Chua HT, Wang X, Teo HY. A numerical study of the Hampson-type miniature Joule–Thomson cryocooler. Int J Heat Mass Transfer 2006;49(3–4):582–93.
[9] Radebaugh R, O'Gallagher A. Regenerator operation at very high frequencies for microcryocoolers. Adv Cryog Eng 2006;823:1919–28.
[10] Garaway I, Grossman G. A study of a high frequency miniature reservoir-less pulse tube. Adv Cryog Eng 2008;52:1547–54.
[11] Garaway I, Gan Z, Bradley P, Veprik A, Radebaugh R. Development of a miniature 150 Hz pulse tube cryocooler. In: Proceedings of the 15th international cryocooler conference; June 2008. p. 105–13.
[12] Chen H, Yang L, Cai J, Liang J, Zhou Y. Application of high frequency miniature pulse tube cryocoolers. Jixie Gongcheng Xuebao/Chin J Mech Eng 2008;44(7):143–6.
[13] Cha JS. Hydrodynamic parameters of micro porous media for steady and oscillatory flow: application to cryocooler regenerators. Doctoral thesis. Georgia Institute of Technology; 2007.
[14] Cha JS, Ghiaasiaan SM, Kirkconnell CS. Longitudinal hydraulic resistance parameters of cryocooler and Stirling regenerators in periodic flow. Adv Cryog Eng 2008;53:259–66.
[15] Cha JS, Ghiaasiaan SM, Kirkconnell CS. Oscillatory flow anisotropic hydrodynamic parameters of microporous media applied in pulse tube and Stirling cryocooler regenerators. Exp Therm Fluid Sci 2008;32(6):1264–78.
[16] Clearman WM. Measurement and correlation of directional permeability and Forchheimer's coefficient of micro porous structures used in pulse-tube cryocoolers. Masters thesis. Georgia Institute of Technology; 2007.
[17] Clearman WM, Cha JS, Ghiaasiaan SM, Kirkconnell CS. Anisotropic steady-flow hydrodynamic parameters of microporous media applied to pulse tube and Stirling cryocooler regenerators. Cryogenics 2008;48(3–4):112–21.
[18] Harvey JP. Oscillatory compressible flow and heat transfer in porous media-application to cryocooler regenerators. Doctoral thesis. Georgia Institute of Technology; 2003.
[19] Kuwahara F, Nakayama A, Koyama H. A numerical study of thermal dispersion in porous media. J Heat Transfer 1996;118(3):756–61.
[20] Kuwahara F, Shirota M, Nakayama A. A numerical study of interfacial convective heat transfer coefficient in two-energy equation model for convection in porous media. Int J Heat Mass Transfer 2001;44(6):1153–9.
[21] Nakayama A, Kuwahara F, Umemoto T, Hayashi T. Heat and fluid flow within an anisotropic porous medium. J Heat Transfer 2002;124(4):746–53.
[22] Kim S-M, Ghiaasiaan SM. Numerical modeling of laminar pulsating flow in porous media. J Fluid Eng 2009;131(4):041203–12.
[23] Cha JS, Ghiaasiaan SM, Desai PV, Harvey JP, Kirkconnell CS. Multi-dimensional flow effects in pulse tube refrigerators. Cryogenics 2006;46(9):658–65.
[24] Nam K, Jeong S. Investigation of oscillating flow friction factor for cryocooler regenerator considering cryogenic temperature effect. Cryogenics 2006;45(12):733–8.
[25] Shen QQ, Ju YL. A new correlation of friction factor for oscillating flow regenerator operating at high frequencies. Adv Cryog Eng 2008;52:267–74.
[26] Gambit users manual. Fluent Inc.; 2003.
[27] Pedras M, De Lemos M. Macroscopic turbulence modeling for incompressible flow through undeformable porous media. Int J Heat Mass Transfer 2001;44(6):1081–93.
[28] Landrum E. Anisotropic parameters of mesh fillers relevant to miniature cryocoolers. Masters thesis. Georgia Institute of Technology; 2009.
[29] Hsu C. Handbook of porous media. 2nd ed. Boca Raton: Taylor and Francis Group; 2005.
[30] Hsu C, Fu H, Cheng P. On pressure–velocity correlation of steady and oscillating flows in regenerators made of wire screens. J Fluid Eng 1999;121:52–6.
[31] FLUENT 6 users manual. Fluent Inc.; 2003.